ELSEVIER

Modeling dendrite density from magnetic resonance diffusion measurements

Sune N. Jespersen,[a,*] Christopher D. Kroenke,[b] Leif Østergaard,[a]
Joseph J.H. Ackerman,[b,c,d] and Dmitriy A. Yablonskiy[b,e]

[a]*Center of Functionally Integrative Neuroscience, Aarhus University Hospital–Århus Sygehus, Nørrebrogade 44, Building 30, 8000 Århus C, Denmark*
[b]*Department of Radiology, Washington University, St. Louis, Missouri 63110, USA*
[c]*Department of Chemistry, Washington University, St. Louis, Missouri 63110, USA*
[d]*Department of Internal Medicine, Washington University, St. Louis, Missouri 63110, USA*
[e]*Department of Physics, Washington University, St. Louis, Missouri 63110, USA*

Diffusion-weighted imaging (DWI) provides a noninvasive tool to probe tissue microstructure. We propose a simplified model of neural cytoarchitecture intended to capture the essential features important for water diffusion as measured by NMR. Two components contribute to the NMR signal in this model: (i) the dendrites and axons, which are modeled as long cylinders with two diffusion coefficients, parallel (D_L) and perpendicular (D_T) to the cylindrical axis, and (ii) an isotropic monoexponential diffusion component describing water diffusion within and across all other structures, i.e., in extracellular space and glia cells. The model parameters are estimated from 153 diffusion-weighted images acquired from a formalin-fixed baboon brain. A close correspondence between the data and the signal model is found, with the model parameters consistent with literature values. The model provides an estimate of dendrite density from noninvasive MR diffusion measurements, a parameter likely to be of value for understanding normal as well as abnormal brain development and function.

Introduction

Although diffusion-weighted imaging is by now a well-established clinical tool, especially in the diagnosis of acute stroke (Moseley et al., 1990), its detailed biophysical underpinnings remain only partially understood. In stroke, for example, the origin of the observed acute decrease in the apparent diffusion coefficient (ADC) has received no satisfactory explanation so far, but more fundamentally, a detailed theory of the relation between the diffusion signal and the underlying tissue structure at the cellular level in a given type and state of tissue is still lacking. During the typical diffusion experiment, with a diffusion time Δ of 20–80 ms, the average water molecule probes a length scale on the order of 5 to 20 μm, making diffusion sensitive to a wide range of microstructural and physiological parameters in the tissue. The ultimate goal of a MR diffusion theory is to relate these microstructural and physiological parameters quantitatively to the diffusion-weighted MR signal. However, deducing the values of these parameters from the MR signal constitutes a complex inverse problem requiring careful modeling of the diffusion signal over a wide range of diffusion times and diffusion weightings (*b*-factors). Despite these challenges, the efforts will undoubtedly be worthwhile. Indeed, the prospect of noninvasively measuring quantitative cytoarchitectural parameters, for example neuron density, dendrite density and neuropil volume fraction, can be anticipated to have a significant impact on a broad range of research areas such as brain mapping (Schleicher et al., 1999), postnatal ontogeny (Amunts et al., 1997), comparative neuroanatomy (Sherwood et al., 2004; Zilles et al., 1986), and be of great value in the study of microstructural changes underlying various pathologies, such as schizophrenia (Colon, 1972), Alzheimer's disease (Stark et al., 2005), and alcoholism (Tang et al., 2004). In addition, histologic studies of neurodegenerative changes during aging have indicated a loss of neurons and dendrites (Stark and Pakkenberg, 2004), and a means to noninvasively characterize these variables *in vivo* would shed considerable light on the aging nervous system.

Here, we develop a simple, analytical model based on three fundamental experimental observations: first, the diffusion signal from gray matter and white matter is not monoexponential (Assaf and Cohen, 1998; Buckley et al., 1999; Le Bihan et al., 1991; Mulkern et al., 1999; Niendorf et al., 1996), suggesting compartmentalization of water. Second, the time independence of the ADC (Clark et al., 2001; Le Bihan et al., 1993; Moonen et al.,

1991; van Gelderen et al., 1994, see however Assaf and Cohen, 1998; Horsfield et al., 1994) for long diffusion times (larger than 20 ms) strongly suggests that the sizes of such cellular compartments are either much larger than the corresponding diffusion length—5–10 μm or they are much smaller such that their contribution to the ADC is zero for all practically achievable diffusion times. Third, the water permeability of cell membranes (and hence compartmentalization) of water differs by orders of magnitude, and most of this variability reflects the differential expression of aquaporin water channels (Borgnia et al., 1999; Solenov et al., 2004). The predominant CNS aquaporin family, aquaporin-4, has recently been found to be almost exclusively expressed in astrocytes (Amiry-Moghaddam and Ottersen, 2003). Neurons and especially neuronal processes (dendrites and axons) – with ion fluxes being closely linked to their active conductivity – are likely the dominant compartment for restricted diffusion, as commonly assumed in models of white matter water diffusion. In gray matter, we hence develop a model where water diffusion is primarily restricted by dendrites (0.1–2 μm diameter, hundreds of micrometers long (Stuart et al., 1999)), fulfilling the dimension requirements above.

The approach is thus to replace the immensely complex surroundings of the water molecules with a simplified structural model of neural tissue intended to capture the salient features of importance to diffusion. One of the most important and well-appreciated features of molecular diffusion in the brain is the diffusion anisotropy. It exists in both white matter and gray matter and is due to the presence of cells with long cylindrical processes— dendrites and axons (see Fig. 1). In our model this population of cells is described as a collection of long impermeable cylinders specified by their density and orientational distribution. A distribution of cylinders was used previously to model diffusion properties of biological tissues (airways of the lung (Yablonskiy et al., 2002), dendrites in a study of NAA diffusion (Kroenke et al., 2004), white matter fiber tracts (Anderson, 2005; Assaf et al., 2004; Sen and Basser, 2005; Szafer et al., 1995; Tournier et al., 2004)). Diffusion of water not associated with the cylinders in our approach is modeled as isotropic Gaussian diffusion, and is intended to approximate the diffusion of water in extracellular space as well as inside glia cells. The underlying assumption is that the water molecules have time to diffuse back and forth between glia cells and extracellular space, the diffusion coefficient thereby reflecting the average properties of both compartments. A promising aspect of the present model is that it allows experimental access to several cytoarchitectural parameters noninvasively, one of the more interesting being the dendrite density. This is a physiological variable that plays a central role in normal brain function and development, and as such would be of great value for monitoring the progress of several diseases of the central nervous system.

Although many experimental studies currently analyze data in terms of the diffusion tensor model, such an approach is strictly speaking valid only for a "quasi-free" diffusion that can be described in terms of anisotropic Gaussian propagator (i.e., anisotropic microscopic viscosity). This is generally not the case in biological tissues where cell membranes impose restrictions or hindrances to molecular diffusion. This is evident in high *b*-factor experiments, where the diffusion signal as a function of *b*-value displays a clear deviation from monoexponential decay (Assaf and Cohen, 1998; Buckley et al., 1999; Le Bihan et al., 1991; Mulkern et al., 1999; Niendorf et al., 1996), in contrast to a simple exponential behavior ($S \sim \exp(-b\,\mathrm{ADC})$) predicted for free diffusion. Attempts to improve the model generally adopt one of two strategies: a "data modeling" approach is to introduce new model parameters that enable increased agreement between the model and the data, and the physical approach is to generate a geometrical model of the underlying tissue and calculate the corresponding MR signal. Examples of the data modeling strategy include adding an additional exponential function with a separate diffusion constant representing a second compartment, the so-called biexponential diffusion model (e.g., Refs. Assaf and Cohen, 1998; Buckley et al., 1999; Le Bihan et al., 1991; Mulkern et al., 1999; Niendorf et al., 1996). A related framework is the so-called Kärger model (Jorg Karger, 1988), which is the biexponential diffusion model with non-local exchange between the two underlying compartments: these models may often be considered as compact ways to summarize the data without a direct interpretation of the model parameters (Chin et al., 2002), except in a few special cases (Sukstanskii et al., 2004; Sukstanskii and Yablonskiy, 2002). The cumulant expansion is also an example
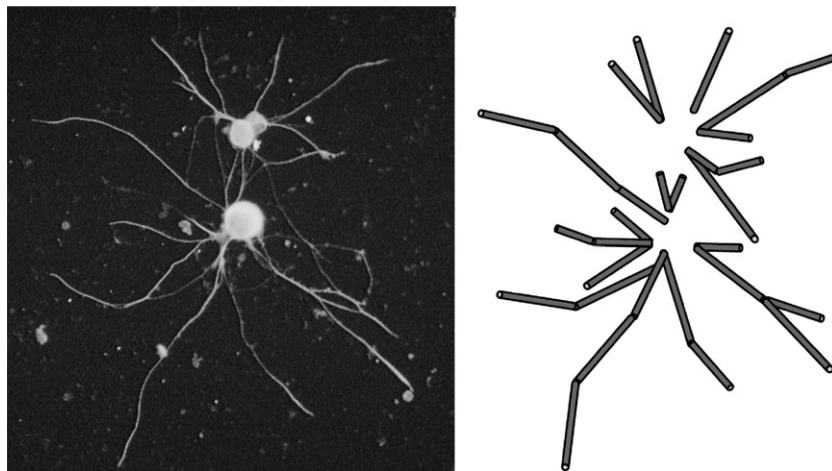

Fig. 1. On the left is a fluorescence microscopy image of a few neurons from an *Aplysia* (reprinted with permission from M. Miller and M. Kirk, The Institute of Neurobiology, University of Puerto Rico), and to the right the corresponding representation in the model, replacing dendrites and axons with cylinders.

of the data modeling approach, although attempts have been made recently to relate the parameters to the underlying tissue microstructure (Frohlich et al., 2006). A different approach was proposed by Yablonskiy et al. (2003) where the influence of the variability in the tissue cellular structure on MR signal was described in terms of a "statistical" model. This phenomenological method provides an accurate account of the diffusion attenuated MR signal dependence on b-value for all brain tissues. In this more empirical vein we note that a non-monoexponential MR diffusion signal behavior, which is well fit to a biexponential, has been observed for the *intracellular* water of *Xenopus* oocytes (Sehy et al., 2002), obviously in the complete absence of dendrites. Further, Kroenke et al. (2006) have shown that high quality diffusion MR data sets from fixed baboon brain can be well characterized without invoking multiple or high order diffusion tensor models. These findings argue for caution in employing highly parameterized descriptions of the MR diffusion signal in the absence of strong biophysical justification.

One of the first studies to analyze a physical model of water diffusion in biological tissue was presented by Latour et al. (1994) where an effective medium theory for diffusion in erythrocytes was analyzed to calculate the diffusion constant at short and long diffusion times. An analytical model concerned explicitly with water diffusion in neural tissue modeled as a regular lattice of cylinders was developed by Szafer et al. (1995), where approximate expressions for the longtime diffusion constants were provided. Cylinders were also used to model restricted diffusion in axons in a composite model presented by Assaf et al. (2004) of hindered and restricted diffusion in fiber tracts. Stanisz et al. (1997) proposed an analytical model of diffusion in optic nerve approximating glia cells and neurons by spheres and prolate ellipsoids respectively allowing water exchange in a modified Kärger approach. Recently, Sen and Basser (2005) presented a model of diffusion in white matter taking into account both the membrane and myelin sheath of axons modeled as cylindrical tubes. The compromise between loss of physical intuition for increased robustness in the face of heterogeneous tissue microstructure (the data modeling approach) and increased physical understanding at the expense of generality to multiple tissue types (the physical approach) affects each of the above studies. The primary contribution of this work is to propose a new model for diffusion in brain tissue based on physical principles and prior knowledge of tissue microstructure. Expressions are derived that allow simultaneous determination of the intra-voxel distribution of fiber orientations while measuring the intracellular diffusion coefficient (not the "apparent diffusion coefficient").

Theory

As described in the introduction, the diffusion signal $S(\mathbf{q}, \Delta)$, is modeled as arising from two separate, non-exchanging components, one from compartments with cylindrical symmetry (dendrites and axons), $S_c(\mathbf{q}, \Delta)$, and one from a compartment with spherical (isotropic) symmetry, $S_i(\mathbf{q}, \Delta)$. Summing up the contribution from both components, the total diffusion signal is

$$S(\mathbf{q}, \Delta)/S_0 = (1 - v)S_i(\mathbf{q}, \Delta) + vS_c(\mathbf{q}, \Delta) \qquad (1)$$

Here, $\mathbf{q} = \gamma\delta\mathbf{g}$ is the diffusion wave vector, γ is the magnetogyric ratio, $\mathbf{g}$ is the diffusion gradient, δ is the duration of the diffusion

gradients, Δ is the time between the leading edges of the two diffusion gradients, $b = \mathbf{q}^2(\Delta - \delta/3)$, S_0 is the signal amplitude at $b = 0$, v is the dendrite associated water volume fraction, and S_c is the signal component arising from molecules in a collection of cylindrically symmetric structures. We consider each of the two terms in Eq. (1) in turn, starting with $S_i(\mathbf{q}, \Delta)$. As a first approximation, the diffusion of water molecules not associated with the cylinders is modeled as isotropic Gaussian diffusion, i.e., a monoexponential diffusion signal with a scalar diffusion constant D_{eff}. It is assumed that during the course of the diffusion experiment, water molecules in this compartment can freely sample extracellular space as well as noncylindrical intracellular space, such as glia cells. This is arguably a rough first approximation, but nevertheless, it turns out to describe the data very well. The effective diffusion constant D_{eff} experienced by water molecules in this compartment therefore reflects the tortuosity of the extra-cylindrical space as well as increased viscosity inside glia cells and hindrances imposed by their cell membranes. The approximation is therefore that $S_i(\mathbf{q}, \Delta) \approx \exp(-bD_{eff})$.

Next, we consider the signal contribution S_c from dendrites and axons. First, a local model of diffusion within cylinders is presented. Heterogeneity in the distribution of cylinder orientations is then modeled using a spherical harmonic expansion.

On a local level, it is assumed that neuronal processes can be described as a collection of long cylinders (see Fig. 1) with a longitudinal diffusion coefficient D_L and a transverse diffusion coefficient $D_T < D_L$. It is assumed that on the timescale of a typical diffusion experiment, the processes are nearly impermeable to water: this is necessary in order to enforce the strict compartmentalization required for the signal to be written as a sum of two contributions. On the other hand, it is assumed that the diffusion time is large enough and $q \equiv |\mathbf{q}|$ small enough (Callaghan et al., 1979) to allow for a Gaussian approximation of the propagator for diffusion inside the cylinders, such that in the narrow pulse approximation for a spin echo experiment each cylinder contributes

$$S_{cyl}(\mathbf{q}, \Delta) \propto \exp(-b(D_L\cos^2\theta' + D_T\sin^2\theta')) \qquad (2)$$

to the total signal, with $D_T \sim r_c^2/\Delta$ for a cylinder of radius r_c and θ' the angle between $\mathbf{g}$ and the cylinder axis. In practice, D_T will reflect the combined effects of cylinder bending, nonvanishing permeability, and possibly water outside the processes experiencing cylindrical diffusion symmetry. Note that the mathematical treatment of the cylindrical diffusion process is only approximate, since interactions of the water molecules with the boundary will add non-Gaussian corrections to the signal expression. Nevertheless, the approximation is accurate for $D\Delta \gg r_c^2$ and $q \ll 1/r$, and in our experiments, the strongest of these conditions corresponds to $r_c \ll 1.6$ μm for the largest $\mathbf{q}$ applied. Note that there is no assumption regarding the Gaussian nature of the propagator itself, only of the signal such that $S_{cyl}(\mathbf{q}_\perp, \Delta) \propto \exp(-\text{constant} \cdot q_\perp^2 r_c^2)$.

In order to arrive at an expression for S_c, it is necessary to sum the signal S_{cyl} from each cylinder in Eq. (2) over all possible orientations. In brain tissue, heterogeneous collections of cylinder orientations are encountered. The orientations of a collection of cylinders in a given voxel are described by $f(\theta, \varphi)d\Omega$, the fraction of dendrites or axons in the solid angle $d\Omega$ specified by spherical polar angles θ and φ in the laboratory frame. In the white matter fiber tracts, the distribution of cylinders tends to peak along the

direction of the fiber tract (Anderson, 2005; Tournier et al., 2004), whereas in gray matter, $f(\theta, \varphi)$ tends to be closer in appearance to a sphere. In general, $f(\theta, \varphi)$ can be expanded in spherical harmonics $Y_{lm}(\theta, \varphi)$ (Laplace series):

$$f(\hat{\mathbf{n}}) = f(\theta, \varphi) = \sum_{lm} f_{lm} Y_{lm}(\theta, \varphi) \qquad (3)$$

where $\hat{\mathbf{n}}$ is the unit vector corresponding to the direction specified by θ and φ, i.e., $\hat{\mathbf{n}} = (\cos\varphi\sin\theta, \sin\varphi\sin\theta, \cos\theta)$. Two properties of the cylinder distributions, namely inversion symmetry, $f(\theta, \varphi) = f(\pi - \theta, \varphi \pm \pi)$, and conjugate symmetry $f(\theta, \varphi) = f^*(\theta, \varphi)$ (the asterisk denotes complex conjugation), impose two constraints on the expansion parameters: f_{lm} is nonzero only if l is even, and $f_{lm} = (-1)^m f_{l-m}^*$, respectively. In addition, the total volume fraction of cylinders equals $v\sqrt{\pi}f_{00}$, since the total mass of all high order spherical harmonics equals 0. Hence, a logical choice is $f_{00} = 1/\sqrt{\pi}$. From this discussion it is also clear that all higher order terms in the expansion contribute a total number of zero cylinders, that is, a positive number in some directions and a negative number in other directions. When summing over all spherical harmonics with nonvanishing coefficients, the number of cylinders in any direction must be positive, but terminating the series at any finite l, may in principle give rise to a net negative number of cylinders in any particular direction. This is, of course, unphysical, but it is completely analogous to the Gibbs ringing phenomenon that arises in Fourier transform theory due to a finite number of harmonics.

The expression for S_c is derived using Eqs. (2) and (3) in the Appendix, where it is found that the signal as a function of b-value and gradient direction (θ, φ), is described by the following equation:

$$S(b, \theta, \varphi) = S_0 \big[(1 - v)e^{-bD_{\text{eff}}} + v\pi e^{-bD_T} \cdot \sum_{l,m} f_{lm} C_l(b(D_L - D_T)) Y_{lm}(\theta, \varphi) \big] \qquad (4)$$

In principle, the sum over l runs from 0 to infinity, but for any practical application, the series must be truncated at some $l = L$. The functions C_l are known exactly for all l, and their appearance as well as some of their properties is discussed in the Appendix. The free parameters to be determined from the data are thus S_0, v, D_{eff}, D_L, D_T and f_{lm}. For $L = 2$, we have explicitly

$$
\begin{aligned}
S(b, \theta, \varphi) = {} & S_0(1 - v)e^{-bD_{\text{eff}}} + S_0 v\pi e^{-bD_T} \Bigg\{ f_{00} \sqrt{\frac{\pi}{b(D_L - D_T)}} \\
& \times \text{erf}\left(\sqrt{b(D_L - D_T)} \right) Y_{00}(\theta, \varphi) + \Bigg[\sqrt{\frac{\pi}{4b(D_L - D_T)}} \\
& \times \text{erf}\left(\sqrt{b(D_L - D_T)} \right) \left(\frac{3}{2b(D_L - D_T)} - 1 \right) \\
& - \frac{3}{2b(D_L - D_T)} e^{-b(D_L - D_T)} \Bigg] \sum_m f_{2m} Y_{2m}(\theta, \varphi) \Bigg\} \qquad (5)
\end{aligned}
$$

with a total of 10 free parameters to be estimated in each voxel.

Methods

Experiments

Data were collected from an immersion-fixed brain from a two-day old baboon, obtained from the Southwest Foundation for Biomedical Research, San Antonio, TX (courtesy of J.J. Neil and T. Inder). The brain was placed within a small container of 4% paraformaldehyde, which in turn was placed inside a cylindrical container of a perfluorinated liquid (product name Krytox, DuPont, Deepwater, NJ), and the experiment was performed at ambient magnet bore temperature of 18 °C. The sample was inserted into a 7-cm i.d. quadrature RF coil ("Litz Cage", Doty Scientific, Colombia, SC), and diffusion-weighted images were then acquired with a Varian Inova MR scanner (Palo Alto, CA) equipped with a 4.7 T magnet (Oxford Instruments, Oxford, UK) and a 10-cm i.d. 3-axis gradient coil system (Magnex Scientific, Oxford, UK) capable of magnetic field gradients of up to 60 G/cm.

One hundred and fifty three diffusion-weighted images were acquired using a standard spin echo diffusion-weighted pulse sequence (Stejskal and Tanner, 1965) with a nonselective 180° pulse. A nonselective 180° pulse was chosen to avoid interference between diffusion and slice-selective gradients. This is important for two reasons: first, it made the calculation of b-factors and the corresponding directions much more straightforward. More importantly, ambiguities in the definition of the diffusion time were avoided. Signal from unwanted echo pathways was suppressed by phase cycling and the diffusion gradients. The imaging parameters were: 64×64 data matrix, field of view 6.4 cm $\times$ 6.4 cm, slice thickness 1.0 mm, TR/TE = 1.3 s/67 ms, and the number of averages was 2. The total imaging time was approximately 7 h. The diffusion parameters were $\delta/\Delta = 5$ ms/50 ms, and 17 b-factors ranging linearly from 0.88 to 15 ms/μm^2. For each b-factor, 9 different orientations were selected from one hemisphere of an 18 point spherical 5-design (Hardin and Sloane, 1996), and this scheme was randomly rotated for each b-factor. A spherical t-design can be considered as a way to equally distribute points on the sphere, with the special property that its use as an equal weight numerical integration scheme is exact for spherical harmonics up to and including $l = t$. As a result of this procedure, 153 unique diffusion directions were obtained with a dense coverage of the unit sphere.

The acquired images were phased using a Bayesian phasing algorithm (http://bayesiananalysis.wustl.edu), and all subsequent analysis was done on the real images. Model fitting and parameter estimation was done with Matlab (The MathWorks, Inc., Natick, MA) using a nonlinear least squares algorithm. Voxels within a manually selected ROI enclosing the entire brain with surrounding formalin were used for data analysis. Finally, a sensitivity analysis was performed by calculating the predicted ADC and FA change in the primary motor cortex and corpus callosum resulting from a 10% change in the model parameters. The ADC and FA were calculated by fitting the DTI model to the signal calculated at $b = 0$ and $b = 3.3$ μm^2/ms ($b \cdot \text{ADC} \approx 1$) using 12 directions corresponding to the vertices of an icosahedron.

Simulations

Our data suggest that terminating the Laplace series at $L = 2$ provides an adequate fit to all 153 data points over most regions of the brain. To assess the utility of the second order Laplace expansion in describing anisotropic diffusion, three simulations with model cylinder distribution functions were performed. An angular distribution shaped like an ellipsoid, containing 1000 cylinders was created, and the diffusion signal as a function of the 153 b-factors described above was calculated. The axes of the

Table 1
The input parameter values of the simulations are compared with the average values found by fitting the model function using 100 realizations of the noise

	S_0	v	$D_L/(\mu m^2/ms)$	$D_T/(\mu m^2/ms)$
Input: primary motor cortex	1.00	1.00	0.65	0.131
Fit	1.04±0.03	0.94±0.05	0.61±0.04	0.133±0.003
Input: corpus callosum	1.00	1.00	0.99	0.0613
Fit	1.05±0.04	0.92±0.06	0.90±0.07	0.062±0.001
Input: crossing corpus callosa	1.00	1.00	0.99	0.0613
Fit	1.07±0.04	0.90±0.06	0.89±0.06	0.063±0.001

The uncertainties are standard deviations.

ellipsoidal distributions were taken to reflect the eigenvalues of a DTI-fit to the data in two regions of interest, the primary motor cortex and the corpus callosum, see Table 3. Each cylinder was taken to have diffusion coefficients D_L and D_T as determined from the fit of our own model in those regions, see Table 1 for details. These scenarios correspond to a fractional anisotropy FA of approximately 0.40 in the corpus callosum and 0.21 in the primary motor cortex. The third test case was two corpus callosum distributions placed at right angles to represent crossing fibers. Random Gaussian noise was added resulting in a signal to noise

ratio of 100, similar to the experiments. Finally, the simulated data sets from 100 noise realizations were fit to the model using the same procedure as with the above described experimental data.

Results

Simulations

The simulated data sets are compared with the model fits in Fig. 2, and the values of the fitting parameters are listed in Table 1. The reconstructed distribution functions are shown in Fig. 3 along with the input elliptical distribution functions.

Experiments

In Fig. 4, Akaikes Information Criterion (AIC) (Akaike, 1974) for the proposed model ($L=2$ in Fig. 4a and $L=4$ in Fig. 4b) is compared with the AIC of a few other models in common use: the standard DTI model (Fig. 4c), the two-component DTI/biexponential tensor model (Fig. 4d), and the tensor cumulant expansion (Fig. 4e). Akaikes Information Criterion provides a way of comparing the quality of different models in describing the data, penalizing increased numbers of parameters in a suitable way. It is related to the χ^2 by $AIC = \chi^2 + 2p$, where p denotes the number of model fit parameters. The AIC is therefore a dimensionless number and, like χ^2, the larger the AIC, the less appropriate the model. The average
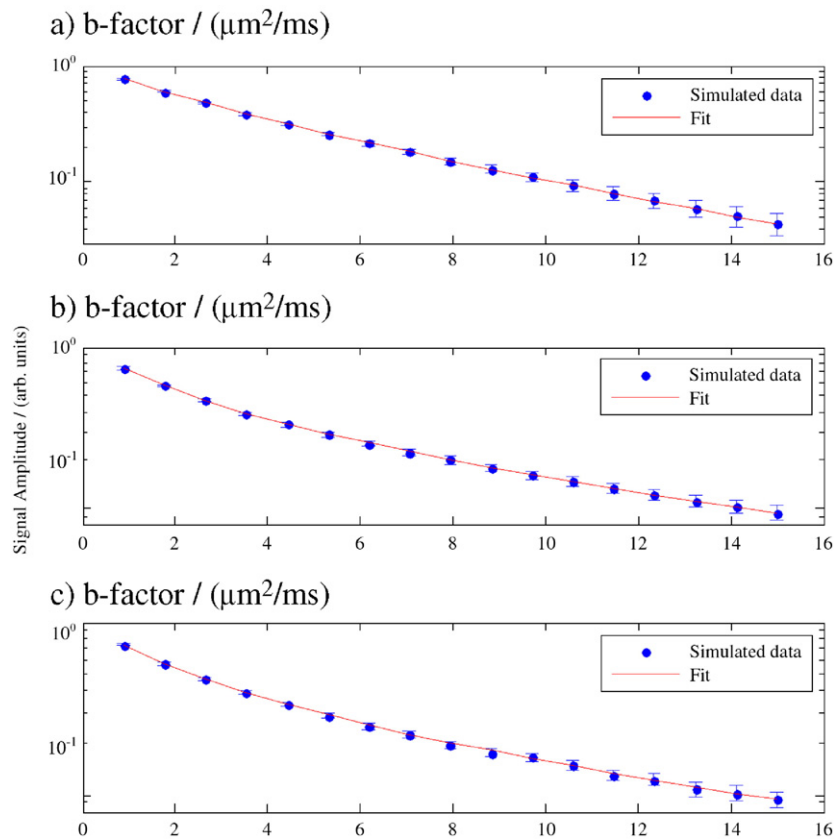

Fig. 2. Comparison of fit with data from computer simulations of 3 model cylinder distributions (see the text for details): (a) primary motor cortex, (b) corpus callosum and (c) two mutually perpendicular corpus callosa. Only the orientationally averaged data over 9 directions corresponding to 17 different b-factors are shown, whereas all 153 data points were used in the fit. In addition, the values of both the fit and the data have been averaged over 100 realizations of noise.
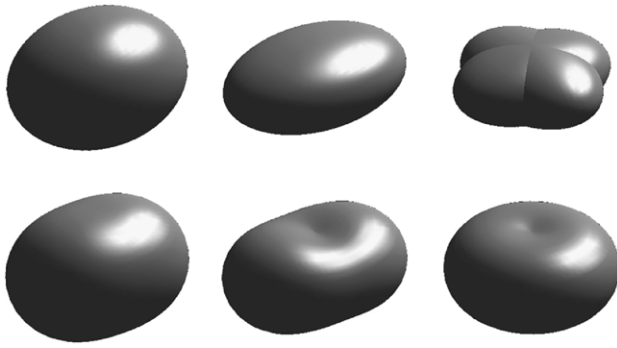
Fig. 3. Cylindrical distribution functions used in the simulations. The top row is the input distribution functions: (a) primary motor cortex, (b) corpus callosum, and (c) crossing of two corpus callosa at right angles. The bottom row is the corresponding distribution functions reconstructed from the fitted parameter values.

SNR on the least b-factor images is about 100, and about 5 on the largest b-factor images. Fig. 5 displays the values of the estimated model parameters as determined by the nonlinear least squares fit. Fig. 5a depicts the cylindrical volume fraction v, Fig. 5b the effective diffusion constant D_{eff}, Fig. 5c is the parallel intra-cylindrical diffusion coefficient, and finally Fig. 5d is an image of D_T, the transverse diffusion coefficient in the cylinders. The intensity scales of Figs. 5b–d have been adjusted for optimum contrast over the brain. For comparison, we provide the parameter maps of the DTI fit in Fig. 6: Fig. 6a is the ADC map and Fig. 6b is the FA map. As a further comparison we also examine the

correlation between the DTI parameters ADC to D_T (Fig. 7a) and FA to AI (Fig. 7b), an anisotropy index for our model. It is defined as

$$AI = \sqrt{\frac{\int d\theta d\varphi \sin\theta |f(\theta,\varphi) - f_{00} Y_{00}|^2}{\int d\theta d\varphi \sin\theta |f(\theta,\varphi)|^2}} = \sqrt{1 - \frac{|f_{00}|^2}{\sum_{l,m} |f_{lm}|^2}} \qquad (6)$$

i.e., essentially the square root of the angular variance divided with the square root of the angular mean square of the cylinder distribution, analogous to FA. Moreover, AI is rotationally invariant and bounded between 0 and 1, being 0 for a completely isotropic distribution and 1 for extremely anisotropic distributions, e.g., AI=1 for a cylinder. In Fig. 8 the cylinder distribution functions $f(\theta, \varphi)$ are reconstructed pixel by pixel corresponding to the region shown in the inset in the upper left corner. The individual distributions have been scaled so that their maximum excursions from 0 (the center of each pixel) are equal. The color coding reflects the original magnitude in any direction, and the corresponding number is therefore proportional to the number of cylinders in that direction. There are very few negative values. A T2-weighted image was used to approximately identify several anatomical regions of interest (ROIs), which were then copied to the diffusion-weighted images as shown in Fig. 9. The corresponding average model parameters with standard errors are listed in Table 2 for the present model and Table 3 for the DTI model. Furthermore, the model parameters in the same anatomical ROIs have been compared statistically in Fig. 10, where 5% Bonferroni corrected confidence intervals are plotted. Finally, Fig. 11 displays a bar graph of the outcome of the sensitivity analysis using values from the primary
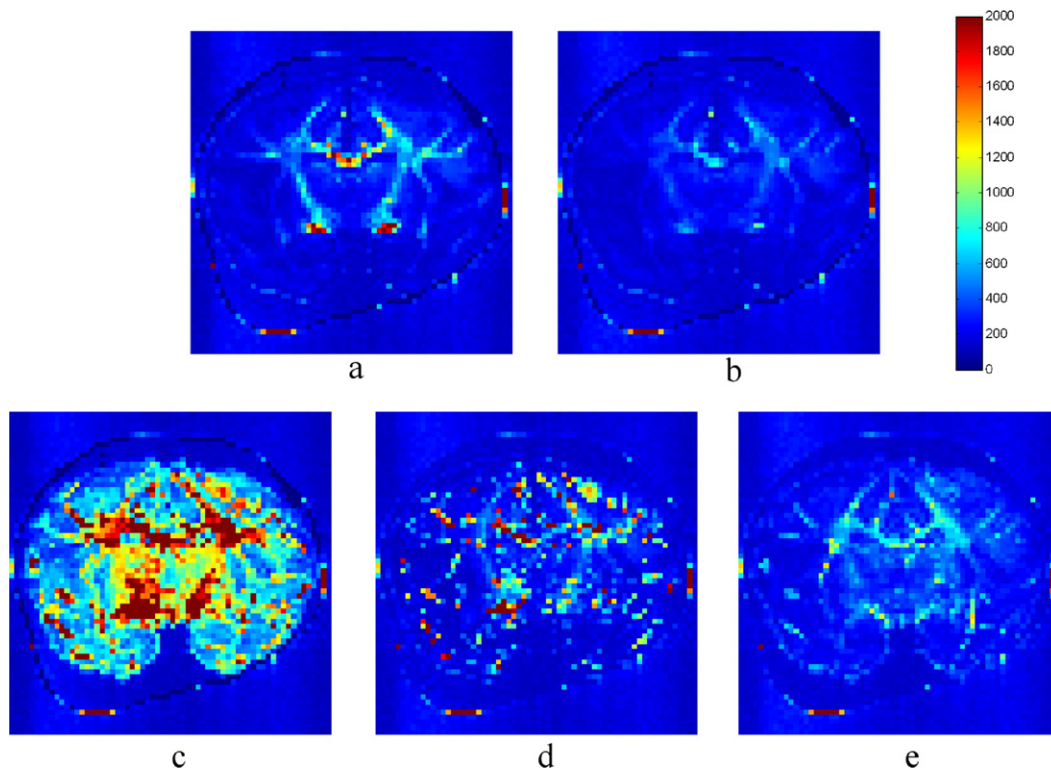

Fig. 4. Akaikes Information Criterion (AIC) of the current model, cut off at $L=2$ (a), cut off at $L=4$ (b) compared to the AIC for the standard DTI model (c), the biexponential DTI model (d), and the tensor cumulant model (e). The line delineating the brain and the formalin corresponds closely to the ROI used for fitting. Outside this ROI, the intensity reflects the noise.
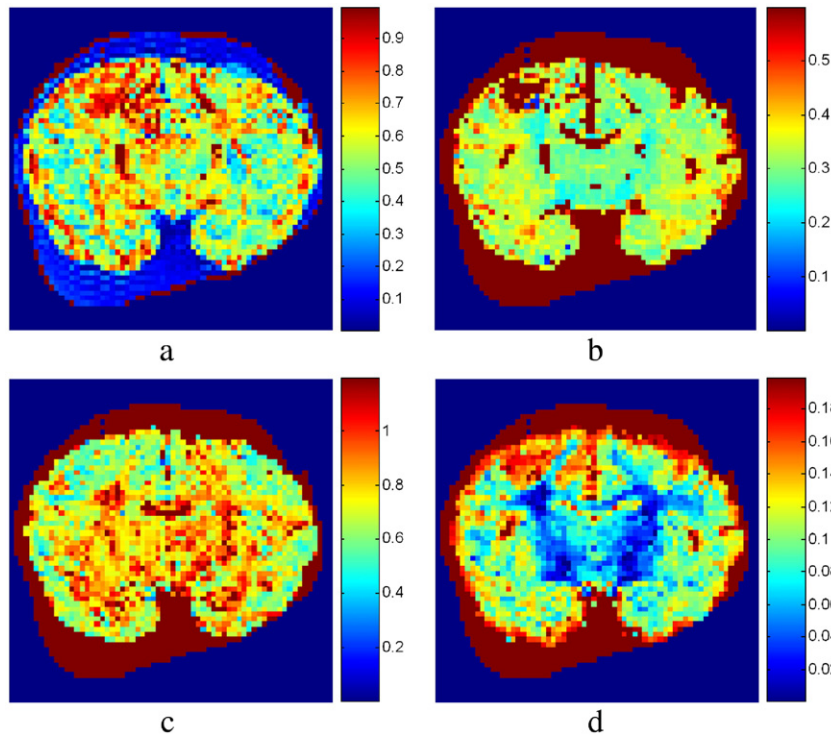
Fig. 5. Images of the estimated model parameters: (a) v, the cylindrical (dendrite/axon) volume fraction, (b) D_{eff}, (c) D_L, and (d) D_T. The image intensity scale has been adjusted for optimal contrast across the brain.

motor cortex in the top row and corpus callosum in the bottom row. Each bar shows the relative change in the ADC (Fig. 11a) and FA (Fig. 11b) arising from a plus (black) or minus (white) 10% change in the corresponding variable.

Discussion

Simulations

The simulations were mainly performed to analyze the effect of terminating the Laplace series at $L=2$. In all cases, the estimated model parameters in Table 1 correspond closely to the input parameters, although the error is somewhat larger for the crossing fibers. From Fig. 2, the fit can be seen to be in convincing agreement with the data; note also the strong non-monoexponential nature of both data and model. Using only $l=0$ and $l=2$ order spherical harmonics, there is obviously a limit to the accuracy with which the cylinder distributions can be reproduced. However, it can be seen from Fig. 3 that in the primary motor cortex and corpus callosum cases, the reproduced distribution functions are qualitatively accurate, whereas the crossing corpus callosa in Fig. 3c are not well resolved. This is simply due to the fact that there are no terms in the $L=2$ Laplace series to describe such geometries; in fact it was demonstrated in Tournier et al. (2004) that fiber populations crossing at 30 degrees could be resolved with a model using $L=8$.

Experiments

Newborn primate brain was chosen for an initial model application because it contains a wide range of tissue types,
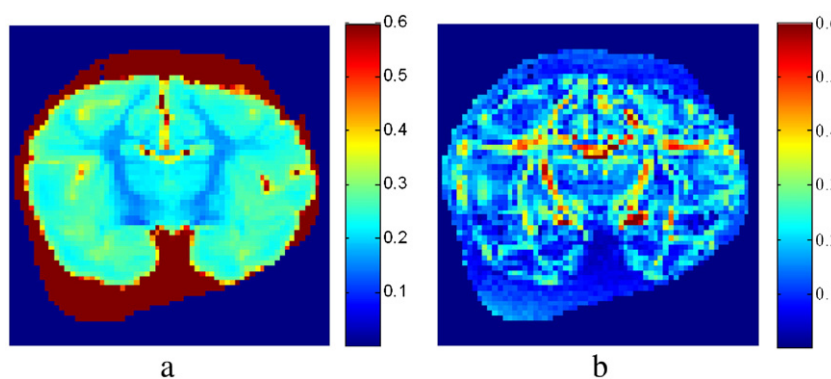

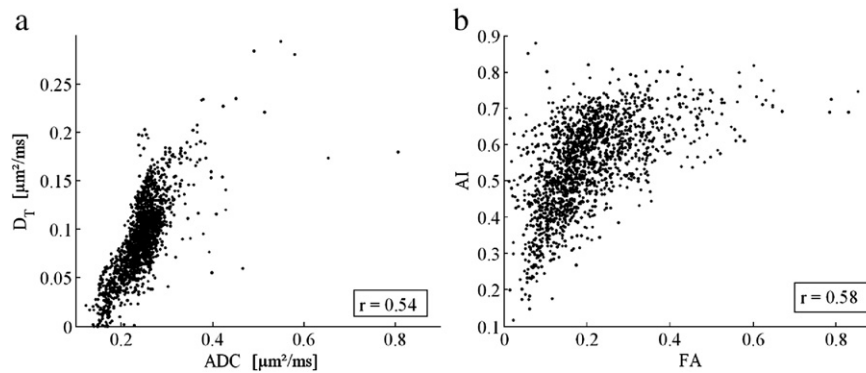Fig. 6. The ADC (a) and the FA (b) from a DTI fit.

Fig. 7. Pixel-by-pixel correlations between the ADC and D_T (a), and between FA and AI (b). Both correlations are highly significant, $p < 5\%$. Only data inside the brain were used.

including white matter at various stages of myelination, cortical and subcortical gray matter. It is clear from Fig. 4 that the present model (Figs. 4a and b) performs much better than the widely used DTI model (Fig. 4c). In fact, the residual signal is comparable to that of the noise over most regions of the brain. However, the AIC image is not equivalent to a pure noise image, in particular, some structure remains in the regions of the major white matter fiber tracts, notably the internal capsule. This is mainly due to the termination of the series at $L=2$, as has been confirmed by a significant decrease in the residuals for a model terminated at $L=4$. Here, however, the focus is on the $L=2$ model to demonstrate its excellent capability to fit all 153 images with only 10 free parameters, whereas the $L=4$ model requires 19. It should nevertheless be noted that going to the next order does not substantially change the estimates of v, D_L, and D_T, but it does improve the description of the orientational variation of the data

with $\mathbf{q}$. The failure of the model to accurately describe white matter cytoarchitecture is, however, not surprising: the extracellular space around white matter fiber bundles, is unlikely to be isotropic. Instead, it will reflect the cylinder symmetry of the tract, violating model assumptions. The biexponential tensor model in Fig. 4d and the tensor cumulant expansion in Fig. 4e both have larger AICs than the $L=2$ model Fig. 4a over most parts of the brain. As explained previously, this means that when considering both residuals and the number of model parameters, the data supports the $L=2$ model over the alternative models in Figs. 4c–e. We note, however, that there is a tendency for the tensor cumulant expansion to perform slightly better in some parts of the major white matter fiber tracts such as the internal capsule and the corpus callosum. This is in good agreement with the inherent limitation of our model in the highly oriented white matter fiber tracts mentioned earlier.
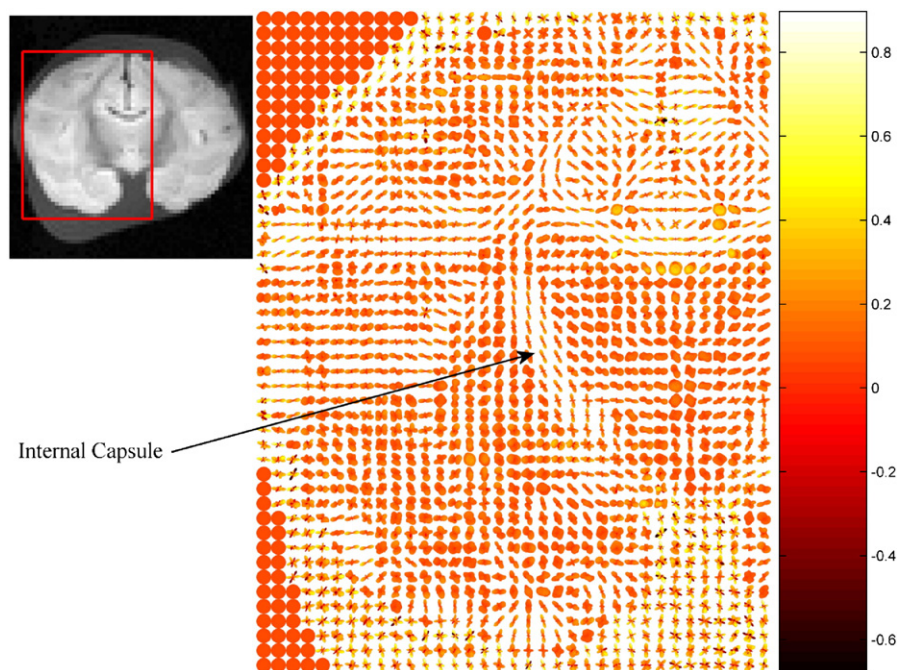

Fig. 8. Based on the values of the expansion coefficients, the cylindrical distribution functions have been reconstructed on a pixel by pixel basis over the region shown in the inset. The distributions have been rescaled individually in each pixel to the same size, and the color coding reflects the original magnitude in any direction, i.e., the number of cylinders in that direction.
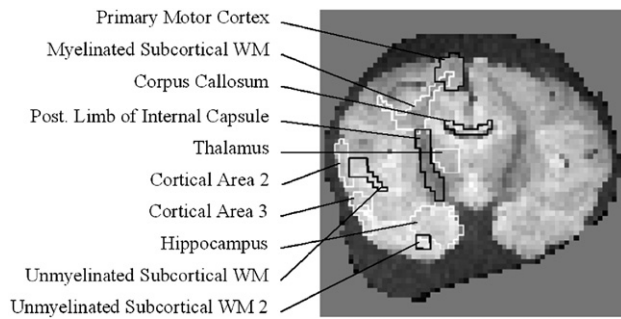
Fig. 9. Definition of the anatomical ROIs used in Table 2. The initial selection was done on a high-resolution T2 weighted image, and the regions were then transformed to the diffusion-weighted image as shown above.

Before discussing the parameter maps in Fig. 5, we note that there is a recurrent "blob" in each of the images in the upper left corner diagonally above the corpus callosum and the left side internal capsule, particularly visible as black in Fig. 5b. We believe that this is due to folding of the formalin containing bag into the image plane. Ideally, the cylindrical component volume fraction v in Fig. 5a should be exactly 0 in the formalin, but the estimated value is close to 0.1. The reason for this discrepancy is presumably due to overfitting, since the diffusion-weighted signal from this region disappears much more rapidly into the noise floor than within the brain tissue. Constraining v to be exactly 0 in this region provides an excellent fit for the formalin without changing D_{eff} substantially, as expected. The dendrite volume fraction shows relatively complex contrast across the brain: there is a thin superficial layer of relatively high volume fraction, followed by an extended subcortical region of somewhat lower values, and finally in the deeper brain regions the cylindrical volume fraction increases again. This parameter should not be confused with the total cellular volume fraction of approximately 0.8, as the latter contains contributions from cell soma and glia cells. Sherwood et al. (2004) measured the volume fraction of cell bodies (glia and neurons) in the primary motor cortex of anthropoid primates by Nissl staining, and found a value of approximately 15% in a 10-year-old baboon. This leaves a neuropil volume fraction of about 85% and subtracting 20% volume fraction occupied by the extracellular space, a rough estimate of $v \approx 65\%$ is obtained. This compares favorably to the value of 0.72 found here (cf., Table 2). Note

however that previous studies have shown a tendency for v to increase with the maturation of the central nervous system (Amunts et al., 1997). Differential T2 weighting may be expected to influence the estimation of the cylindrical volume fraction, since intracellular transverse relaxation presumably is faster than extracellular relaxation, and this effect is likely to cause an underestimation of the intracellular volume fraction. It is however unclear exactly how this influences v, as both compartments in this model have intracellular constituents.

The effective diffusion constant D_{eff} has a value of approximately 1.8 μm^2/ms in the formalin (note that all experiments were performed at room temperature), and this is in close agreement with the ADC found with a single exponential fit in the same region. In the brain, D_{eff} is substantially lower: in the internal capsule, it has a value of about 0.2 μm^2/ms, and everywhere else it is about 0.3 to 0.5 μm^2/ms. The sharply reduced value as compared with the formalin reflects tortuosity λ due to impermeable dendrites, cellular hindrances, and intracellular (glia) viscosity. If the tortuosity $\lambda = 1.6$ (Nicholson, 2001) of the extracellular space alone would be responsible, a value of about $D_{free}/\lambda^2 \approx 0.7$ μm^2/ms would be predicted. Note, however, that the tortuosity value of 1.6 is due to all cellular constituents when the diffusion length is larger than the granularity of the tissue, whereas the tortuosity due to neuronal dendrites alone is smaller.

The parallel cylindrical diffusion constant D_L averages to approximately 0.8 μm^2/ms, slightly less than half of the diffusion constant in the formalin. In reference Kroenke et al. (2004) investigated the diffusion of N-acetyl-L-aspartate (NAA) in human and rat brain. NAA is an intracellular metabolite, and may therefore serve as an endogenous probe of neuronal intracellular space. The authors argued that intracellular viscosity was the dominant determinant of D_L, and estimated this viscosity to be roughly twice that of a temperature-matched dilute aqueous solution. Despite microanatomical alterations in fixed post-mortem tissue, our results are in good agreement with this, since under these assumptions the ratio of D_L in the brain to D_{eff} in the formalin is the ratio of the viscosities. The numbers found from the fit would thus entail a viscosity ratio of 2.25 (intracellular space to aqueous solution). Similar information was recently presented in Zhao et al. (2006) for the intracellular diffusion constant in HeLa cells.

Even though D_T is much smaller than the other diffusion constants of the model, its inclusion turns out to be vital for the quality of the fit. Its value averages about 0.1, with a substantially

Table 2
Average parameter values with standard errors for some anatomical regions of interest as outlined in Fig. 9

Region of interest	S_0	v	$D_{eff}/(\mu m^2/ms)$	$D_L/(\mu m^2/ms)$	$D_T/(\mu m^2/ms)$
Corpus callosum	31.8±0.5	0.70±0.05	0.46±0.08	0.99±0.07	0.061±0.005
Myelinated Subc. wm	25.7±0.3	0.67±0.02	0.39±0.06	0.83±0.03	0.058±0.006
Post. Limb Int. capsule	21.5±0.3	0.74±0.03	0.69±0.10*	0.81±0.02	0.036±0.003
Unmyelinated Subc. wm	31.1±0.3	0.53±0.02	0.33±0.01	0.66±0.03	0.089±0.004
Unmyelinated Subc. wm2	35.6±0.5	0.63±0.07	0.29±0.03	0.83±0.06	0.11±0.01
Cortical area 2	28.2±0.2	0.74±0.03	0.47±0.07	0.70±0.03	0.137±0.005
Cortical area 3	31.1±0.3	0.64±0.03	0.56±0.10	0.69±0.04	0.128±0.005
Hippocampus	33.6±0.2	0.57±0.02	0.40±0.03	0.82±0.03	0.115±0.004
Primary motor cortex	26.1±0.3	0.72±0.03	0.44±0.05	0.65±0.03	0.131±0.005
Thalamus	28.1±0.3	0.61±0.02	0.295±0.002	0.79±0.02	0.069±0.003

Some names have been abbreviated for reasons of space; subc wm=subcortical white matter and Post. Limb Int. capsule=the posterior limb of the internal capsule. (*) This value is strongly influenced by what appears to be an anomaly in the image, c.f. Fig. 5b. Disregarding this small region, the value is approximately 0.02 μm^2/ms.

Table 3
Average parameter values for the DTI model in the same anatomical regions as Table 2

Region of interest	ADC	FA	λ_1	λ_2	λ_3
Corpus callosum	0.24±0.08	0.40±0.15	0.34±0.10	0.23±0.10	0.15±0.08
Myelinated Subc. wm	0.20±0.03	0.26±0.11	0.26±0.03	0.19±0.04	0.14±0.04
Post. Limb Int. capsule	0.16±0.02	0.33±0.14	0.23±0.03	0.14±0.03	0.12±0.03
Unmyelinated Subc. wm	0.24±0.02	0.20±0.06	0.28±0.03	0.23±0.02	0.19±0.02
Unmyelinated Subc. wm2	0.26±0.01	0.17±0.06	0.30±0.03	0.25±0.02	0.21±0.01
Cortical area 2	0.27±0.04	0.27±0.08	0.36±0.07	0.25±0.04	0.22±0.04
Cortical area 3	0.27±0.03	0.16±0.09	0.32±0.05	0.26±0.03	0.23±0.03
Hippocampus	0.27±0.03	0.14±0.06	0.31±0.03	0.27±0.03	0.24±0.03
Primary motor cortex	0.27±0.09	0.21±0.08	0.33±0.09	0.26±0.09	0.23±0.09
Thalamus	0.21±0.01	0.13±0.04	0.24±0.01	0.21±0.01	0.19±0.01

lower value in white matter regions, e.g., 0.03 in the internal capsule, see Table 2. This result may seem counterintuitive because in the white matter fiber tracts, the cylinders, i.e., the myelinated axons, presumably have larger radii than in the gray matter, and the existence of the myelin insulation is known to present a strong diffusion barrier, consequently minimizing the axon permeability to water. The result, however, can be understood based on the assumption that D_T reflects higher bending curvature and nonvanishing permeability of the processes in the gray matter as compared to white matter. D_T is the diffusivity showing the strongest correlation to the DTI diffusivities. This is demonstrated in the scatter plot of Fig. 7a, where each point represents one pixel, its x-coordinate corresponding to the ADC-value and y-coordinate being the D_T-value: there is an approximate and statistically significant linear correlation between the two parameters. In the Results section, we introduced a rotationally invariant measure of anisotropy for our model, and in Fig. 7b this parameter is

correlated with the FA measure from the DTI fit. Again, a very nice statistically significant linear correlation is observed, demonstrating that the two parameters reflect similar information.

Callaghan et al. (1979) and Yablonskiy et al. (2002) derived an approximate relationship between the low b-factor ADC and D_L and D_T; ADC$=1/3(D_L+2D_T)$. In the present context, this is generalized to ADC$=v/3(D_L+2D_T)+(1-v)D_{eff}$, and using the values from Table 2, an ADC of approximately 0.34 is predicted in the primary motor cortex, comparing favorably to the ADC value of 0.3 derived from the DTI fit, see Table 3.

The appearance of the spherical harmonics expansion parameters, f_{2m} (not shown), reveals significant structure, in particular outlining the white matter fiber tracts. The values of the expansion parameters in each pixel are combined using Eq. (3) to produce the pixelwise distribution of cylinders in Fig. 8. The overall qualitative behavior appears to be in agreement with known white matter architecture. In particular, the pathway of the internal capsule is
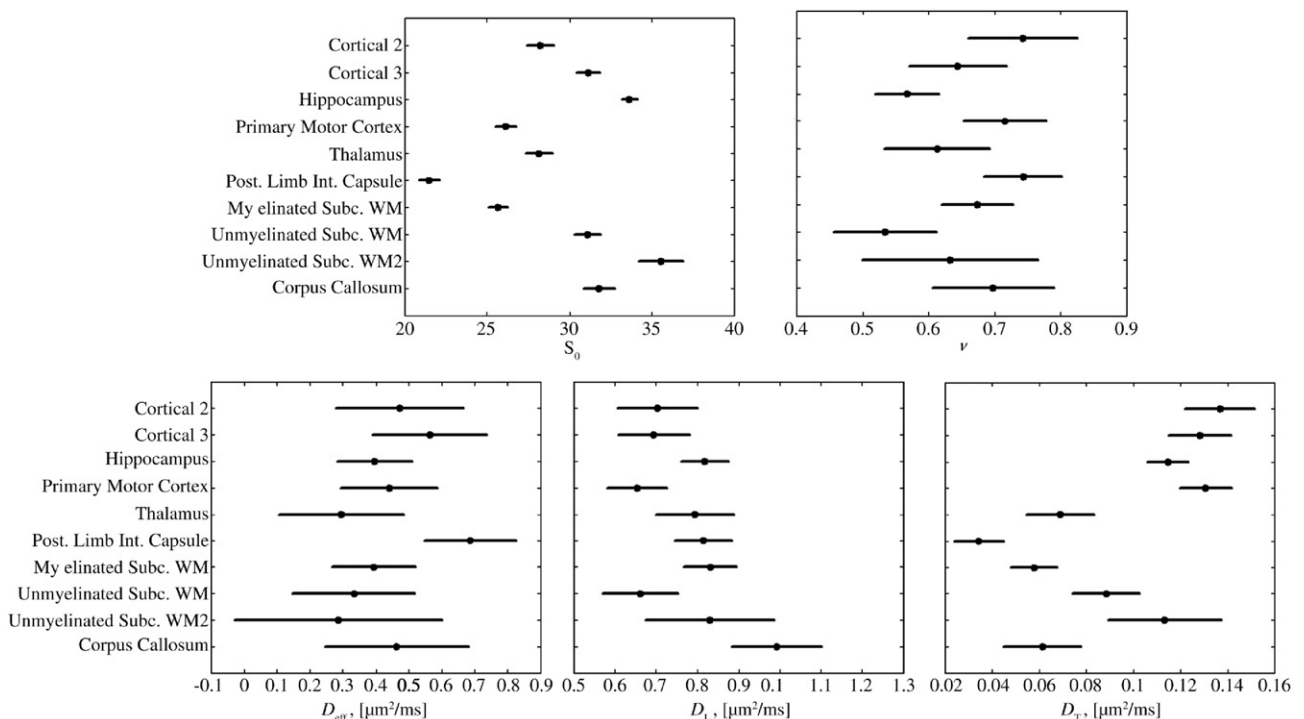

Fig. 10. 5% confidence intervals (Bonferroni corrected) for the model parameters in the anatomical ROIs defined in Fig. 9.

clearly visible. In addition, a radial orientational tendency is noted in the cortical areas, a phenomenon also observed in immature cortical gray matter (Mori et al., 2001; Neil et al., 1998). In other regions, somewhat incoherent orientations are found; this may be due to partial volume effects and degrading effects of fixation. Furthermore, as revealed by the simulations, regions with fiber crossings will not be resolved reliably with a second order Laplace expansion.

In Fig. 10 we compare the means of S_0, v, D_{eff}, D_L, D_T in the anatomical ROIs defined in Fig. 9 using a Bonferroni-corrected multiple comparison procedure. The signal intensity evidently presents a good variable for segmenting the different brain regions. The dendrite density, on the other hand, covers a broad range of different values in each ROI, and this is in accordance with the fact that each anatomical region contains different layers having different cytoarchitecture. The isotropic diffusion constant presents relatively little contrasts across the ROIs, and the same is the case for the intracellular diffusivity, indicating that water motion in neurons is similar across the entire brain. The transverse diffusivity shows significant variations, in particular between gray matter and white matter.

It is tempting to speculate about possible cellular mechanisms underlying the observed ADC deficit in acute stroke in the context of the current model. To assist such considerations, the response in the ADC and FA to changes in the model parameters were calculated and plotted in Fig. 11, based on the values in the primary motor cortex and corpus callosum. There is no pronounced sensitivity to any one parameter, perhaps indicating that the ADC decrease is the result of several pathological changes. A relative increase in the dendritic volume fraction leads to a decrease in the ADC, but in reality such a change would have to be balanced by its effect on the value of the transverse diffusion constant. If dendritic swelling increases the diameter of the individual dendrites, this may be expected to increase the transverse diffusivity; however, this counteracts the aforementioned decrease of ADC. At the same time, D_{eff} would presumably decrease due to slower diffusion in the smaller and more tortuous extracellular space. A decrease in the isotropic diffusion constant D_{eff} will also lead to an ADC decrease. Such an effect could be induced by similar decreases in the diffusion constants of either astroglia or extracellular space, but it may also be the result of changes in the relative contribution of those two compartments to D_{eff}. If the intracellular diffusion constant in astrocytes is lower than that of the extracellular space, and if astroglial swelling is realized at the expense of the extracellular space, the result will be a decrease in D_{eff}. The marginally most sensitive parameter in the corpus callosum is the longitudinal diffusion constant D_L, the ADC being an increasing function of this variable. A decrease in this parameter may be brought about by changes in the intracellular milieu, resulting for example in increased dendritic viscosity. Finally, it is possible the ADC changes underlying stroke is the result of significant changes in the permeability of individual membranes. In this case the model should be adjusted to accommodate permeable cylinders. The difference between the bar graphs for the ADC in the primary motor cortex (top) and corpus callosum (bottom) can be explained mainly from the difference in the magnitude of contributions from the cylindrical component, being much larger in the latter.
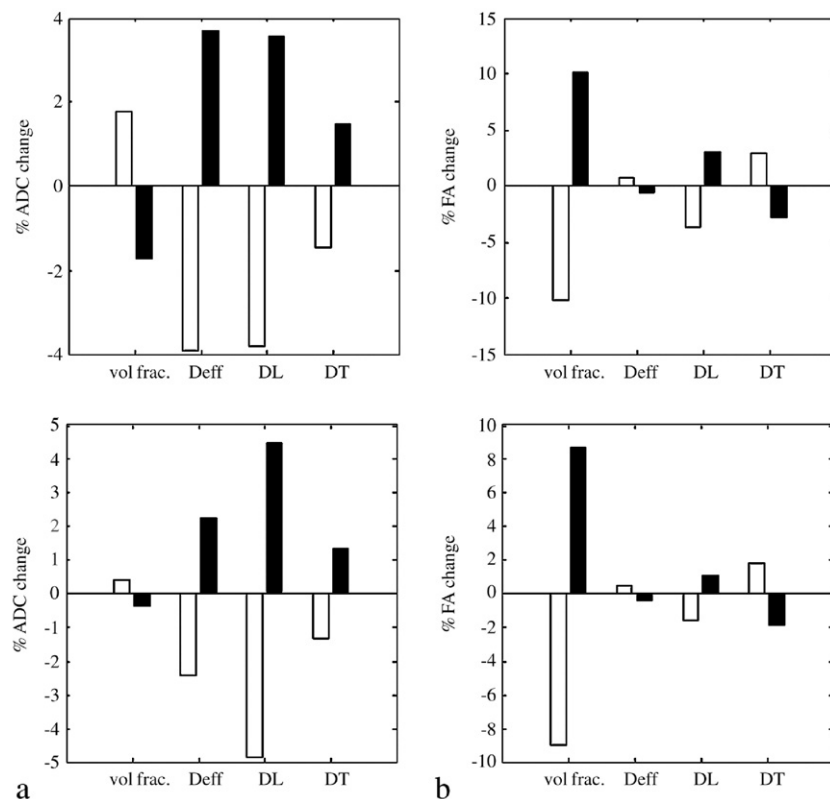

Fig. 11. The response of the ADC (a) and FA (b) to a 10% change in the model parameters for the primary motor cortex (top) and corpus callosum (bottom). The white bar associated with each variable corresponds to a negative increment in that variable, and the black bar to a positive increment.

The FA is clearly quite sensitive to the volume fraction of cylinders, the very source of the anisotropy. This also explains the dependence on the other parameters. We note that dendritic swelling alone would cause the FA to increase, in contrast to experimental observations. Again, however, an isolated change of v would not occur in practice, but would be accompanied by changes in D_{eff} and D_T. A much larger relative decrease in D_T would thus bring the FA to decrease. This picture is quite similar in the two ROIs.

We have demonstrated that the MR diffusion signal can be well modeled by postulating an anisotropic diffusion component derived from a distribution of dendrites (approximated by a distribution of cylinders) within a surrounding isotropic diffusion environment, a component representative of everything else that makes up the tissue microstructure. Here one accepts that current limits on data signal-to-noise may not support more structurally detailed and physiologically insightful models at this time.

Although the present model compares very favorably to the experimental data, there are a number of issues that have not been addressed. Notably among these is the role of water exchange between two tissue components—cylindrical cells and "extra-cylindrical space" (glia and extracellular water), the effect of which will be addressed in a future work. In addition, although the framework captures important aspects of water diffusion in neural tissues, a number of simplifications have been introduced. In particular, the neuron topology and geometry assumed here ignores branching of the dendrites, their bending, and the existence of a distribution of cylinder properties such as diameters and diffusion constants. However, incorporating all of these and other complications would most likely render the present model analytically intractable and hence obscure the biophysical insight gained from an understanding of its behavior. The present model constitutes a reasonable compromise between reflecting the actual biological reality and physical and mathematical simplicity and tractability.

One of the novel features of the current model is that it may provide a means of measuring the local dendrite density noninvasively, a physiological variable that may be of importance in evaluating normal brain development, function and performance. This is a very promising aspect of the proposed model, likely to be of interest to a wide research and clinical community. However, certain practical issues have to be addressed before the framework is applicable to *in vivo* experiments, regarding for example requirements for the diffusion sampling and imaging time. One option, for gray matter regions of interest, could be to sample diffusion in only one direction. From the appearance of Eq. (5) for fixed spherical polar angles, it should still be possible to determine S_0, v, D_{eff}, D_T and D_L due to the unique b-dependence of each of the individual terms in the signal function. However, the expansion coefficients in the cylinder distribution functions will be indeterminate since the spherical harmonics are sampled in only one direction. This is a focus of current efforts.

Conclusion

A theoretical model of diffusion based on an explicit geometrical representation of neural tissue was developed. The model contains two independent components, one with cylindrical symmetry reflecting diffusion in dendrites and axons, and one with isotropic symmetry reflecting diffusion within and across all other structures. By describing the spatial distribution of cylindrical components within a voxel as a second order spherical harmonic expansion, the experimental data – 153 diffusion-weighted images – is modeled quite well in most structures of a neonatal baboon brain. The obtained parameter values compare favorably to literature-derived values and correlate well to DTI parameters. The possibility of measuring dendrite density shows promising potential. While further work is needed to examine and perhaps relax the influence of some of the approximations, the present framework constitutes an important step towards a better understanding of water diffusion in neural tissue.

Appendix A

Here, the expression for S_c, the signal from a collection of cylindrically symmetric structures (dendrites and axons), is derived.

In order to sum Eq. (2) over all cylinder orientations, it is necessary first to relate the spherical polar angles of the diffusion gradients and the cylinder axes in the laboratory frame. Focusing for the moment on a single cylinder, we let θ' and φ' denote the angles of the cylinder axis in a coordinate system S' in which the z'-axis is parallel to $\mathbf{q}$, $\hat{\mathbf{n}}'$ is the corresponding unit vector, and θ and φ are the angles of $\mathbf{q}$ in the laboratory system S. The contribution to the signal from this cylinder is thus $\exp(-b(D_L\cos^2\theta' + \sin^2\theta'))$, and the number of cylinders in this direction is $f(R(\varphi, \theta, 0)\hat{\mathbf{n}}')$, where $R(\varphi, \theta, 0) = R_z(\varphi)R_y(\theta)$ is the rotation that brings S to S' by rotating first θ about the y-axis and then φ about the z-axis. The appearance of the rotation R in the argument of f is essential, since it is the angular coordinates of the cylinders in the laboratory frame S that are sought, whereas $\hat{\mathbf{n}}'$ is specified in S'. In other words, the signal depends on the relative angle between $\mathbf{q}$ and the cylinder axis, but must be expressed in terms of the accessible parameters in the laboratory frame. We employ the convention that rotations connect the same physical point in two different coordinate systems. For example, if $\hat{\mathbf{n}}' = (0, 0, 1)$ in S', associated with a cylinder parallel to $\mathbf{q}$, i.e., the z'-axis, then $\hat{\mathbf{n}}' = R(\varphi, \theta)\hat{\mathbf{n}}' = \mathbf{q}/|\mathbf{q}|$ as it should. Combining these considerations, the signal arising from all cylinders in a given voxel is determined from

$$S_c(\mathbf{q}, \Delta) = \int d\theta' d\varphi' \sin\theta' e^{-b(D_L\cos^2\theta' + D_T\sin^2\theta')} f(R(\varphi, \theta, 0)\hat{\mathbf{n}}'). \quad (7)$$

Here, the integration is over all angles θ' and φ' between the cylindrical axes and the $\mathbf{q}$ vector in S'. In order to proceed, we exploit the well-known rotational properties of the spherical

harmonics being basis functions of the unitary irreducible representation of SO(3), the space of all rotations in R^3:

$$f(R(\varphi,\theta,0)\hat{\mathbf{n}}') = \sum_{lmm'} f_{lm} Y_{lm}(\theta',\varphi') D^l_{mm'}(\varphi,\theta,0)^* \tag{8}$$

Here $D^l_{mm'}$ (Wigner rotation matrices), $l=0, 1,\ldots, m=-1, 1+1,\ldots l$ constitute a unitary irreducible representation of SO(3) (Tinkham, 1964), and combining Eqs. (7) and (8) leads to

$$S_c(\mathbf{q},\Delta) = \sum_{lmm'} f_{lm} D^l_{mm'}(\varphi,\theta,0)^*$$
$$\times \int d\theta' d\varphi' \sin\theta' e^{-b(D_L\cos^2\theta'+D_T\sin^2\theta')} Y_{lm'}(\theta',\varphi')$$
$$= \sum_{lm} f_{lm} D^l_{m0}(\varphi,\theta,0)^* \sqrt{\frac{2l+1}{4\pi}} \pi e^{-bD_T}$$
$$\times \int_{-1}^{1} d\mu e^{-b(D_L-D_T)\mu^2} P_l(\mu) \tag{9}$$

using the relation between spherical harmonics and Legendre functions P_l (Arfken and Weber, 2005). Eq. (9) may be rewritten as

$$S_c(\mathbf{q},\Delta) = \pi e^{-bD_T} \sum_{lm} f_{lm} C_l(b(D_L-D_T)) Y_{lm}(\theta,\varphi) \tag{10}$$

where the functions C_1 are defined by comparison with Eq. (9). In the last step, the identity

$$D^l_{m0}(\varphi,\theta,0)^* = \sqrt{\frac{4\pi}{2l+1}} Y_{lm}(\theta,\varphi) \tag{11}$$

was used, a proof of which can be found in, e.g., Sakurai (1994). The functions C_l are real, nonzero only for even l, and can be calculated exactly for all l. A variety of equivalent representations can be found, a useful one for numerical computations is

$$C_{2n}(x) = \int_{-1}^{1} d\mu P_{2n}(\mu) e^{-x\mu^2}$$
$$= (-1)^n \frac{(2n)!}{n!n!2^{2n}}$$
$$\times \sum_{k=0}^{n} (n+1/2)_k (-n)_k \frac{x^{-k}}{k!}$$
$$\times \left(\sqrt{\frac{\pi}{x}} \mathrm{erf}(\sqrt{x}) - 2e^{-x} \sum_{j=0}^{k-1} \frac{x^j}{(3/2)_j} \right) \tag{12}$$

where the Pochhammer symbols are used for notational convenience (Arfken and Weber, 2005):

$$(a)_k = a\cdot(a+1)\ldots(a+k-1), \ (a)_0 \equiv 1 \tag{13}$$

Alternatively, a more compact form is

$$C_{2n}(x) = (-x)^n \frac{\Gamma(n+1/2)}{\Gamma(2n+3/2)} M(n+1/2, 2n+3/2, -x) \tag{14}$$

where $M(a, b, x) = {}_1F_1(a, b, x)$ is a confluent hypergeometric function (Arfken and Weber, 2005). The limiting behavior is

$$C_{2n}(x) \sim \begin{cases} (-1)^n \frac{(2n)!}{2^{2n}n!n!} \sqrt{\frac{\pi}{x}}, & x\to\infty \\ \frac{\Gamma(n+1/2)}{\Gamma(2n+3/2)} (-x)^n, & x\to 0 \end{cases} \tag{15}$$
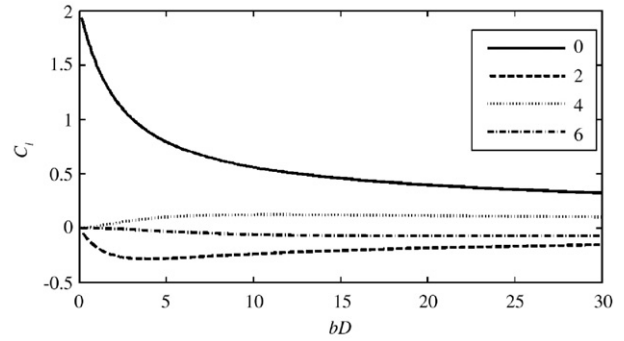

Fig. 12. Graph of the first 4 C_l functions as described in the text. The only function that has physical meaning by itself is C_0, reflecting the diffusion signal from an isotropic arrangement of cylinders. All higher order C_l can be negative as well as positive, and all start from zero. Moreover, the absolute values are bounded above by C_0.

to leading order, and a graph of the first few functions can be seen in Fig. 12. The first two C_l functions are given explicitly below:

$$C_0(x) = \sqrt{\frac{\pi}{x}}\mathrm{erf}(\sqrt{x}) \text{ and}$$
$$C_2(x) = \sqrt{\frac{\pi}{4x}}\mathrm{erf}(\sqrt{x})\left(\frac{3}{2x}-1\right) - \frac{3}{2x}e^{-x} \tag{16}$$

The first of these equations is identical to one found by Yablonskiy et al. (2002) for diffusion of He3 in the airways of the lungs, and used by Kroenke et al. (2004) for the description of N-acetyl-L-aspartate (NAA) diffusion in human and rat brain. The inclusion of this term alone produces a signal that is macroscopically isotropic, but the detailed form of which reflects the underlying microscopic anisotropy due to the dendrites. As can also be seen from Eq. (15), the decay of this term is strongly non-monoexponential, in accordance with experimental observations.

References

Akaike, H., 1974. New look at statistical-model identification. IEEE Trans. Automat. Contr. AC19, 716–723.

Amiry-Moghaddam, M., Ottersen, O.P., 2003. The molecular basis of water transport in the brain. Nat. Rev., Neurosci. 4, 991–1001.

Amunts, K., Schmidt-Passos, F., Schleicher, A., Zilles, K., 1997. Postnatal development of interhemispheric asymmetry in the cytoarchitecture of human area 4. Anat. Embryol. (Berl) 196, 393–402.

Anderson, A.W., 2005. Measurement of fiber orientation distributions using high angular resolution diffusion imaging. Magn. Reson. Med. 54, 1194–1206.

Arfken, G.B., Weber, H.J., 2005. Mathematical Methods for Physicists, 6th ed. Elsevier, Boston.

Assaf, Y., Cohen, Y., 1998. Non-mono-exponential attenuation of water and N-acetyl aspartate signals due to diffusion in brain tissue. J. Magn. Reson. 131, 69–85.

Assaf, Y., Freidlin, R.Z., Rohde, G.K., Basser, P.J., 2004. New modeling and experimental framework to characterize hindered and restricted water diffusion in brain white matter. Magn. Reson. Med. 52, 965–978.

Borgnia, M., Nielsen, S., Engel, A., Agre, P., 1999. Cellular and molecular biology of the aquaporin water channels. Annu. Rev. Biochem. 68, 425–458.

Buckley, D.L., Bui, J.D., Phillips, M.I., Zelles, T., Inglis, B.A., Plant, H.D., Blackband, S.J., 1999. The effect of ouabain on water diffusion in the rat

hippocampal slice measured by high resolution NMR imaging. Magn. Reson. Med. 41, 137–142.

Callaghan, P.T., Jolley, K.W., Lelievre, J., 1979. Diffusion of water in the endosperm tissue of wheat grains as studied by pulsed field gradient nuclear magnetic resonance. Biophys. J. 28, 133–141.

Chin, C.L., Wehrli, F.W., Hwang, S.N., Takahashi, M., Hackney, D.B., 2002. Biexponential diffusion attenuation in the rat spinal cord: computer simulations based on anatomic images of axonal architecture. Magn. Reson. Med. 47, 455–460.

Clark, C.A., Hedehus, M., Moseley, M.E., 2001. Diffusion time dependence of the apparent diffusion tensor in healthy human brain and white matter disease. Magn. Reson. Med. 45, 1126–1129.

Colon, E.J., 1972. Quantitative cytoarchitectonics of the human cerebral cortex in schizophrenic dementia. Acta Neuropathol. (Berl.) 20, 1–10.

Frohlich, A.F., Ostergaard, L., Kiselev, V.G., 2006. Effect of impermeable boundaries on diffusion-attenuated MR signal. J. Magn. Reson. 179, 223–233.

Hardin, R.H., Sloane, N.J.A., 1996. McLaren's improved snub cube and other new spherical designs in three dimensions. Discrete Comput. Geom. 15, 429–441.

Horsfield, M.A., Barker, G.J., McDonald, W.I., 1994. Self-diffusion in CNS tissue by volume-selective proton NMR. Magn. Reson. Med. 31, 637–644.

Jorg Karger, 1988. Principles and application of self diffusion measurements by nuclear magnetic resonance. Adv. Magn. Reson. 12, 1–89.

Kroenke, C.D., Ackerman, J.J., Yablonskiy, D.A., 2004. On the nature of the NAA diffusion attenuated MR signal in the central nervous system. Magn. Reson. Med. 52, 1052–1059.

Kroenke, C.D., Bretthorst, G.L., Inder, T.E., Neil, J.J., 2006. Modeling water diffusion anisotropy within fixed newborn primate brain using Bayesian probability theory. Magn. Reson. Med. 55, 187–197.

Latour, L.L., Svoboda, K., Mitra, P.P., Sotak, C.H., 1994. Time-dependent diffusion of water in a biological model system. Proc. Natl. Acad. Sci. U. S. A. 91, 1229–1233.

Le Bihan, D., Moonen, C.T., van Zijl, P.C., Pekar, J., DesPres, D., 1991. Measuring random microscopic motion of water in tissues with MR imaging: a cat brain study. J. Comput. Assist. Tomogr. 15, 19–25.

Le Bihan, D., Turner, R., Douek, P., 1993. Is water diffusion restricted in human brain white matter? An echo-planar NMR imaging study. NeuroReport 4, 887–890.

Moonen, C.T., Pekar, J., de Vleeschouwer, M.H., van Gelderen, P., van Zijl, P.C., DesPres, D., 1991. Restricted and anisotropic displacement of water in healthy cat brain and in stroke studied by NMR diffusion imaging. Magn. Reson. Med. 19, 327–332.

Mori, S., Itoh, R., Zhang, J., Kaufmann, W.E., van Zijl, P.C.M., Solaiyappan, M., Yarowsky, P., 2001. Diffusion tensor imaging of the developing mouse brain. Magn. Reson. Med. 46, 18–23.

Moseley, M.E., Cohen, Y., Mintorovitch, J., Chileuitt, L., Shimizu, H., Kucharczyk, J., Wendland, M.F., Weinstein, P.R., 1990. Early detection of regional cerebral ischemia in cats: comparison of diffusion- and T2-weighted MRI and spectroscopy. Magn. Reson. Med. 14, 330–346.

Mulkern, R.V., Gudbjartsson, H., Westin, C.F., Zengingonul, H.P., Gartner, W., Guttmann, C.R., Robertson, R.L., Kyriakos, W., Schwartz, R., Holtzman, D., Jolesz, F.A., Maier, S.E., 1999. Multi-component apparent diffusion coefficients in human brain. NMR Biomed. 12, 51–62.

Neil, J.J., Shiran, S.I., McKinstry, R.C., Schefft, G.L., Snyder, A.Z., Almli, C.R., Akbudak, E., Aaronovitz, J.A., Miller, J.P., Lee, B.C.P., Conturo, T.E., 1998. Normal brain in human newborns: apparent diffusion coefficient and diffusion anisotropy measured using diffusion tensor imaging. Radiology 209, 57–66.

Nicholson, C., 2001. Diffusion and related transport mechanisms in brain tissue. Rep. Prog. Phys. 64, 815–884.

Niendorf, T., Dijkhuizen, R.M., Norris, D.G., van Lookeren, C.M., Nicolay, K., 1996. Biexponential diffusion attenuation in various states of brain tissue: implications for diffusion-weighted imaging. Magn. Reson. Med. 36, 847–857.

Sakurai, J.J., 1994. Modern Quantum Mechanics. Addison-Wesley Publishing Company Inc.

Schleicher, A., Amunts, K., Geyer, S., Morosan, P., Zilles, K., 1999. Observer-independent method for microstructural parcellation of cerebral cortex: a quantitative approach to cytoarchitectonics. NeuroImage 9, 165–177.

Sehy, J.V., Ackerman, J.J., Neil, J.J., 2002. Evidence that both fast and slow water ADC components arise from intracellular space. Magn. Reson. Med. 48, 765–770.

Sen, P.N., Basser, P.J., 2005. Modeling diffusion in white matter in the brain: a composite porous medium. Magn. Reson. Imaging 23, 215–220.

Sherwood, C.C., Holloway, R.L., Erwin, J.M., Schleicher, A., Zilles, K., Hof, P.R., 2004. Cortical orofacial motor representation in Old World monkeys, great apes, and humans: I. Quantitative analysis of cytoarchitecture. Brain Behav. Evol. 63, 61–81.

Solenov, E., Watanabe, H., Manley, G.T., Verkman, A.S., 2004. Sevenfold-reduced osmotic water permeability in primary astrocyte cultures from AQP-4-deficient mice, measured by a fluorescence quenching method. Am. J. Physiol.: Cell Physiol. 286, C426–C432.

Stanisz, G.J., Szafer, A., Wright, G.A., Henkelman, R.M., 1997. An analytical model of restricted diffusion in bovine optic nerve. Magn. Reson. Med. 37, 103–111.

Stark, A.K., Pakkenberg, B., 2004. Histological changes of the dopaminergic nigrostriatal system in aging. Cell Tissue Res. 318, 81–92.

Stark, A.K., Pelvig, D.P., Jorgensen, A.M., Andersen, B.B., Pakkenberg, B., 2005. Measuring morphological and cellular changes in Alzheimer's dementia: a review emphasizing stereology. Curr. Alzheimer Res. 2, 449–481.

Stejskal, E.O., Tanner, J.E., 1965. Spin diffusion measurements: spin echoes in the presence of a time-dependent field gradient. J. Chem. Phys. 42, 288–292.

Stuart, G., Spruston, N., Hèausser, M., 1999. Dendrites. Oxford Univ. Press, Oxford, New York.

Sukstanskii, A.L., Yablonskiy, D.A., 2002. Effects of restricted diffusion on MR signal formation. J. Magn. Reson. 157, 92–105.

Sukstanskii, A.L., Yablonskiy, D.A., Ackerman, J.J., 2004. Effects of permeable boundaries on the diffusion-attenuated MR signal: insights from a one-dimensional model. J. Magn. Reson. 170, 56–66.

Szafer, A., Zhong, J., Gore, J.C., 1995. Theoretical model for water diffusion in tissues. Magn. Reson. Med. 33, 697–712.

Tang, Y., Pakkenberg, B., Nyengaard, J.R., 2004. Myelinated nerve fibres in the subcortical white matter of cerebral hemispheres are preserved in alcoholic subjects. Brain Res. 1029, 162–167.

Tinkham, M., 1964. Group Theory and Quantum Mechanics. McGraw-Hill, New York.

Tournier, J.D., Calamante, F., Gadian, D.G., Connelly, A., 2004. Direct estimation of the fiber orientation density function from diffusion-weighted MRI data using spherical deconvolution. NeuroImage 23, 1176–1185.

van Gelderen, P., de Vleeschouwer, M.H., DesPres, D., Pekar, J., van Zijl, P. C., Moonen, C.T., 1994. Water diffusion and acute stroke. Magn. Reson. Med. 31, 154–163.

Yablonskiy, D.A., Sukstanskii, A.L., Leawoods, J.C., Gierada, D.S., Bretthorst, G.L., Lefrak, S.S., Cooper, J.D., Conradi, M.S., 2002. Quantitative in vivo assessment of lung microstructure at the alveolar level with hyperpolarized 3He diffusion MRI. Proc. Natl. Acad. Sci. U. S. A. 99, 3111–3116.

Yablonskiy, D.A., Bretthorst, G.L., Ackerman, J.J., 2003. Statistical model for diffusion attenuated MR signal. Magn. Reson. Med. 50, 664–669.

Zhao, L., Kroenke, C.D., Ackerman, J.J., Neil, J.J., 2006. The Intracellular Water Diffusion Coefficient of Cultured Microbead-Adherent HeLa Cells is $>=1$ $\mu m^2/ms$.

Zilles, K., Armstrong, E., Schlaug, G., Schleicher, A., 1986. Quantitative cytoarchitectonics of the posterior cingulate cortex in primates. J. Comp. Neurol. 253, 514–524.